Chapter 3
Theories of Phonon Transport in Bulk and Nanostructured Solids

G.P. Srivastava

Abstract In this chapter we outline the theories that are usually employed for phonon transport in solids. In particular, we provide a detailed description of the essential steps in deriving the lattice thermal conductivity expressions within the single-mode relaxation-time approximation. Explicit expression for various phonon scattering rates, in bulk and low-dimensional solids, have been provided. Numerical evaluation of scattering rates and the conductivity expressions is detailed using both Debye's isotropic continuum scheme and a realistic Brillouin zone summation technique based upon the application of special phonon wavevectors scheme. Results of the conductivity are presented for selected bulk, superlattice, and nanostructured systems. Based on such results, we briefly discuss the concept of phonon engineering of high-efficiency thermoelectric materials.

3.1 Introduction

Techniques for experimental measurement and theoretical modelling of thermal conductivity in naturally grown bulk soilds have been established since the early 1950s. In this millenium, nanostructures, or meta materials in general, have attracted a great deal of attention. Such materials do not exist in nature but can be fabricated in laboratory using modern growth techniques. However, in general, methods of experimental measurements and theoretical modelling of some properties, including thermal conductivity, of such materials have not yet been well established.

Thermal conduction in insulating and semiconducting solid structures (bulk or low-dimensional forms) is almost exclusively contributed by phonons. A phonon, using the second-quantised notation, is a quantum of atomic vibrational waves in

G.P. Srivastava (✉)
School of Physics, University of Exeter, Stocker Road, Exeter EX4 4QL, UK
e-mail: G.P.Srivastava@exeter.ac.uk

S.L. Shindé and G.P. Srivastava (eds.), *Length-Scale Dependent Phonon Interactions*, Topics in Applied Physics 128, DOI 10.1007/978-1-4614-8651-0_3,
© Springer Science+Business Media New York 2014

crystalline solids and is represented both as a quasi-particle and an elementary excitation of energy $\hbar\omega(\boldsymbol{q}s)$ corresponding to wavevector $\boldsymbol{q}$ and polarisation s. Phonon transport in a given solid is governed by details of dispersion relations (i.e. ω vs. $\boldsymbol{q}$ for all polarisation branches s) and processes that control lifetimes of these quasi-particles. An ideally perfect and purely harmonic solid would exhibit perfect heat conduction, i.e. infinite thermal conductivity, as its atoms can be viewed as executing purely harmonic vibrations, leading to the concept of independent, or non-interacting, phonons of infinitely long lifetime. Real solids are characterised by anharmonic inter-atomic forces and presence of defects. These features limit phonon lifetimes and thus thermal conductivity. In order to estimate phonon lifetimes and thermal conductivity it is important to have a detailed knowledge of phonon dispersion relations for the relevant crystal structure.

Ab initio methods for phonon dispersion calculations have been described in the chapter by Tütüncü and Srivastava, and for phonon lifetimes in bulk semiconductors in the chapters by Garg et al. and Mingo et al. In this chapter we will briefly discuss phonon dispersion relations and their usage in deriving expressions for phonon lifetime contributions from various scattering sources in bulk and nanostructured semiconductors. We will then discuss how these two ingredients can be utilised in numerical calculations of the phonon conductivity in such systems. Finally, we will briefly discuss how changes in the thermal conductivity due to nanostructuring can be engineered for increasing the efficiency (i.e. the figure-of-merit) of thermoelectric materials.

3.2 Phonon Transport Theories

The rate of heat energy flow $\boldsymbol{Q}$ per unit area normal to a finite (but small) temperature gradient ∇T across a solid is given by Fourier's law

$$Q_i = -\sum_j \kappa_{ij} \nabla T_j , \tag{3.1}$$

with the coefficient $\{\kappa_{ij}\}$ known as the thermal conductivity tensor. Accepting this observation, conductivity expressions have been derived by following approaches at two different levels of sophistication. At one level, a statistical mechanical approach, known as the Green–Kubo linear-response approach [1], is used to express κ in terms of the time integral of the heat current autocorrelation function (i.e. canonical-ensemble average with respect to the Hamiltonian of the system) $< \boldsymbol{Q}(t) \cdot \boldsymbol{Q}(0) >$. This approach has been followed both at classical and quantum levels. At another level, κ is expressed by obtaining a solution of a linearised Boltzmann equation satisfied by the phonon distribution function $n_{\boldsymbol{q}s}(\boldsymbol{r}, t)$ in the steady state of heat flow through the solid (see, e.g., [2, 3]). As in general, the phonon Boltzmann equation cannot be solved exactly, several formulations for expressing κ have been

presented [3]. In this section we will provide a brief overview of the theories for the phonon conductivity based on the Green–Kubo's linear-response approach and the Boltzmann equation formulation.

3.2.1 Theories Based on Green–Kubo's Linear-Response Approach

3.2.1.1 Classical Level

At the classical level of the Green–Kubo approach a molecular dynamical simulation is performed in real space (see, e.g., [4, 5]). In this approach, Newton's second law and the kinematic equations of motion are used, based on (semi)classically derived interatomic potential(s), to determine the classical position and momentum space trajectories of a system of particles.

The heat current is written as

$$\boldsymbol{Q} = \sum_i E_i v_i + \frac{1}{2} \sum_{i,j} (\boldsymbol{F}_{ij} \cdot v_i) \boldsymbol{r}_{ij}, \tag{3.2}$$

where E_i, r_i, and v_i are, respectively, the energy, position vector, and velocity of particle i, $\boldsymbol{r}_{ij}$ is the interparticle separation vector, and $\boldsymbol{F}_{ij}$ is the force between particles i and j. For a monatomic bulk crystal, the heat current autocorrelation function is fitted into a functional form

$$\langle \boldsymbol{Q}(t) \cdot \boldsymbol{Q}(0) \rangle = A \exp(-t/\tau), \tag{3.3}$$

where A is a constant and τ is a time constant. The isotropic thermal conductivity expression for a bulk material is then obtained as

$$\kappa = \frac{k_{\mathrm{B}} T^2 N_0 \Omega}{3} A\tau, \tag{3.4}$$

where k_{B} is Boltzmann's constant, $N_0 \Omega$ represents crystal volume (with N_0 unit cells, each of volume Ω). The energy E and force $\boldsymbol{F}$ terms are usually obtained from the use of empirically derived inter-atomic potential. Details on the application of the approach can be found in McGaughey and Kaviany [4], and Huang and Kaviany [6].

3.2.1.2 Quantum Level

At quantum level the heat current is expressed as an operator in the Heisenberg representation

$$\hat{\boldsymbol{Q}}(t) = \frac{1}{N_0\Omega} \sum_{\boldsymbol{q}s} \hbar\omega(\boldsymbol{q}s)\hat{n}_{\boldsymbol{q}s}(t)\boldsymbol{c}_s(\boldsymbol{q}), \tag{3.5}$$

where $\boldsymbol{c}_s(\boldsymbol{q})$ is the velocity of phonon mode $\boldsymbol{q}s$ with frequency $\omega(\boldsymbol{q}s)$ and $\hat{n}_{\boldsymbol{q}s}$ is the phonon number operator

$$\hat{n}_{\boldsymbol{q}s} = \hat{a}^{\dagger}_{\boldsymbol{q}s}\hat{a}_{\boldsymbol{q}s} \tag{3.6}$$

with $\hat{a}^{\dagger}_{\boldsymbol{q}s}$ and $\hat{a}_{\boldsymbol{q}s}$ as phonon creation and annihilation operatores, respectively. The conductivity tensor expression, therefore, reads

$$\kappa_{ij} = \frac{\hbar^2}{N_0\Omega k_{\mathrm{B}}T^2}\Re\int_0^{\infty} \mathrm{d}t \sum_{\boldsymbol{q}\mathrm{s}\boldsymbol{q}'\mathrm{s}'} \omega(\boldsymbol{q}\mathrm{s})\omega(\boldsymbol{q}'\mathrm{s}')c^i_{\mathrm{s}}(\boldsymbol{q})c^j_{\mathrm{s}'}(\boldsymbol{q}')\mathscr{C}_{\boldsymbol{q}\mathrm{s}\boldsymbol{q}'\mathrm{s}'}(t), \tag{3.7}$$

where $c^i_s(\boldsymbol{q})$ is the ith component of the velocity of a phonon mode $\boldsymbol{q}s$ and

$$\mathscr{C}_{\boldsymbol{q}s\boldsymbol{q}'s'}(t) = \langle\hat{a}^{\dagger}_{\boldsymbol{q}s}(t)\hat{a}_{\boldsymbol{q}'s'}(0)\rangle \tag{3.8}$$

is a *correlation function*.

The correlation function $\mathscr{C}_{\boldsymbol{q}s\boldsymbol{q}'s'}(t)$ represents the canonical-ensemble average of the operator $\hat{a}^{\dagger}_{\boldsymbol{q}s}(t)\hat{a}_{\boldsymbol{q}'s'}(0)$ with respect to the total phonon Hamiltonian H of the system:

$$\mathscr{C}_{\boldsymbol{q}s\boldsymbol{q}'s'}(t) = \frac{\mathrm{Tr}(\mathrm{e}^{-\beta H}\hat{a}^{\dagger}_{\boldsymbol{q}s}(t)\hat{a}_{\boldsymbol{q}'s'}(0))}{\mathrm{Tr}(\mathrm{e}^{-\beta H})}, \qquad \beta = 1/k_{\mathrm{B}}T. \tag{3.9}$$

Several techniques have been employed to evaluate the correlation function, including Zwangis–Mori's projection operator method, double-time Green's function method, and imaginary-time Green's function method. Details of the first two methods can be found in Srivastava [3] and of the third method in Ziman [7]. The final solution can be expressed as

$$\mathscr{C}_{\boldsymbol{q}s\boldsymbol{q}'s'}(t) = \delta_{\boldsymbol{q}\boldsymbol{q}'}\delta ss'\bar{n}_{\boldsymbol{q}s}(\bar{n}_{\boldsymbol{q}s}+1)\mathrm{e}^{-t/\tau_{\boldsymbol{q}s}}, \tag{3.10}$$

where $\bar{n}_{\boldsymbol{q}s}$ is the Bose–Einstein distribution function and $\tau_{\boldsymbol{q}s}$ is the relaxation time for a phonon in mode $\boldsymbol{q}s$. The Hamiltonian required for the simulation is usually adopted from empirically chosen inter-atomic potential, but it can be made from first-principles treatments.

3.2.1.3 Extraction of Relaxation Time

An effective relaxation time $\tau_{\boldsymbol{q}s}$ can be obtained for different situations of the change in the Hamiltonian from that for a perfect crystal within harmonic approximation,

e.g. due to the presence of impurities and defects, and crystal anharmonicity. However, there are genuine difficulties in dealing with two situations in particular. Firstly, the contribution towards $\tau_{\boldsymbol{q}s}$ from the presence of isotopic impuries requires the molecular dynamics simulation to be carried out over an excessively large unit cell containing atoms of appropriate atomic masses. Such contributions, therefore, have not yet been included satisfactorily. Secondly, it is not easy to unscramble the anharmonic contribution in the form of separate phonon contributions involved in three-phonon or four-phonon processes. Neither is it easy to establish separate roles of the anharmonic Normal (momentum conserving) and Umklapp (momentum non-conserving) processes.

3.2.2 Theories Based on Phonon Boltzmann Transport Equation

Theories of lattice thermal conductivity based on the Boltzmann transport equation make the basic assumption that the occupation number of a phonon in mode $\boldsymbol{q}s$ is governed by a distribution function $n_{\boldsymbol{q}s}(\boldsymbol{r}, t)$ in the neighbourhood of space position $\boldsymbol{r}$ at time t. In the general form of Boltzmann equation, for a dielectric subjected to a (small) temperature gradient ∇T, the distribution function satisfies the equation

$$-\boldsymbol{c}_s(\boldsymbol{q}) \cdot \nabla T \frac{\partial n_{\boldsymbol{q}s}}{\partial T} + \left.\frac{\partial n_{\boldsymbol{q}s}}{\partial t}\right|_{\text{scatt}} = 0, \tag{3.11}$$

with the second term on the left-hand side representing the rate of change due to phonon scattering mechanisms. The linearised Boltzmann equation

$$-\boldsymbol{c}_s(\boldsymbol{q}) \cdot \nabla T \frac{\partial \bar{n}_{\boldsymbol{q}s}}{\partial T} + \left.\frac{\partial n_{\boldsymbol{q}s}}{\partial t}\right|_{\text{scatt}} = 0, \tag{3.12}$$

represents a physically appealing simplification of Eq. (3.11), where

$$\bar{n}_{\boldsymbol{q}s} = [\exp(\hbar\omega(\boldsymbol{q}s)/k_{\text{B}}T) - 1]^{-1} \tag{3.13}$$

is the Bose–Einstein (or equilibrium) distribution function. Expressions for the term $\partial n_{\boldsymbol{q}s}/\partial t|_{\text{scatt}}$ corresponding to relevant phonon scattering mechanisms must be derived before Eq. (3.12) is solved for $n_{\boldsymbol{q}s}(t)$ and eventually an expression for thermal conductivity is established. In general, phonon scattering mechanisms can be described as *elastic* (in which the participating phonon $\boldsymbol{q}s$ retains its identity) and *inelastic* (in which the participating phonon $\boldsymbol{q}s$ loses its identity). In general, only approximate forms of inelastic scattering rates can be derived. This is particularly the case for phonon scattering due to crystal anharmonic effects. This difficulty has led to two main routes for the derivation of thermal conductivity expression. These will be briefly described here.

3.2.2.1 Variational Principles

The scattering term in Eq. (3.12) can, in general, be expressed as

$$-\frac{\partial n_{\boldsymbol{q}s}}{\partial t}\bigg|_{\text{scatt}} = \sum_{\boldsymbol{q}'s'} P^{ss'}_{\boldsymbol{q}\boldsymbol{q}'} \psi^{s'}_{\boldsymbol{q}'}, \tag{3.14}$$

where $\psi_{\boldsymbol{q}s} (\equiv \psi^s_{\boldsymbol{q}})$ provides a measure of deviation of the phonon distribution function from its equilibrium value

$$\begin{aligned} n_{qs} &= [\exp(\hbar\omega(\boldsymbol{q}s)/k_{\mathrm{B}}T - \psi_{\boldsymbol{q}s}) - 1]^{-1} \\ &\simeq \bar{n}_{\boldsymbol{q}s} - \psi_{\boldsymbol{q}s} \frac{\partial \bar{n}_{\boldsymbol{q}s}}{\partial(\hbar\omega(\boldsymbol{q}s))} \\ &= \bar{n}_{\boldsymbol{q}s} + \psi_{\boldsymbol{q}s} \bar{n}_{\boldsymbol{q}s} (\bar{n}_{\boldsymbol{q}s} + 1), \end{aligned} \tag{3.15}$$

and $P^{ss'}_{\boldsymbol{q}\boldsymbol{q}'}$ are the elements of the phonon collision operator, providing a measure of phonon transition probabilities.

Expressions for the phonon collision operator elements $P^{ss'}_{\boldsymbol{q}\boldsymbol{q}'}$ can be derived by applying time-dependent perturbation theory. The deviation function $\psi_{\boldsymbol{q}s}$ can then be obtained from Eq. (3.12) provided that the inverse of the matrix operator $\{P^{ss'}_{\boldsymbol{q}\boldsymbol{q}'}\}$ exists. Unfortunately, only partial information is available about the nature of the anharmonic part of the collision operator (for detail, see [3, 8]). This leaves $\psi_{\boldsymbol{q}s}$ unknown in the temperature range where the role of crystal anharmonicity plays an important role. The essence of the variational method for lattice thermal conductivity is to treat $\psi_{\boldsymbol{q}s}$ as a trial function. The simplest approximation for the anharmonic contribution to $\psi_{\boldsymbol{q}s}$ is [3, 8]

$$\psi_{\boldsymbol{q}s} = \boldsymbol{q} \cdot \boldsymbol{u}, \tag{3.16}$$

where $\boldsymbol{u}$ is some constant vector parallel to the applied temperature gradient.

Using the trial function in Eq. (3.16) Ziman [2] derived a *lower bound* for the conductivity. By noting and employing the positive semi-definite property of the phonon collision operator P, Benin [9] developed a *sequence of monotonically convergent lower bounds* for the conductivity. The first term in this sequence is the Ziman limit. It was later shown by Srivastava [10] that a *sequence of monotonically convergent upper bounds* for the conductivity can also be developed. In theory, an estimate for the exact conductivity can then be confined to a small difference between an upper bound and a lower bound. An improved estimate of any conductivity bound can be made by adopting scaling and Ritz procedures [11]. The concept of obtaining both a lower bound and an upper bound for estimating a desired (but inherently unknown) quantity is called *complementary variational principles*, details of which can be found in the book by Arthurs [12].

3.2.2.2 Relaxation-Time Theories

The difficulty in expressing the scattering rate in Eq. (3.12) in terms of a possible solution for the deviation function $\psi_{\boldsymbol{q}s}$ requiring consideration of the phonon collision operator P in its full form is usually dealt with the introduction of the concept of phonon *relaxation time*. This is achieved by expressing

$$-\left.\frac{\partial n_{\boldsymbol{q}s}}{\partial t}\right|_{\text{scatt}} = \frac{n_{\boldsymbol{q}s} - \bar{n}_{\boldsymbol{q}s}}{\tau_{\boldsymbol{q}s}}, \tag{3.17}$$

where $\tau_{\boldsymbol{q}s}$ is the relaxation time for a phonon in mode $\boldsymbol{q}s$. It should, however, be made clear that this expression is based upon a big simplifying assumption, is subject to a fundamental criticism, and is valid under certain conditions. The criticism is that the concept of relation time of a phonon mode becomes invalid in describing its participation in multi-phonon scattering events involving phonon creation and annihilation. Notwithstanding this criticism, the expression above assumes the concept of a single-mode relaxation time. To explain this point let us consider three phonons $\boldsymbol{q}s, \boldsymbol{q}'s'$ and $\boldsymbol{q}''s''$ involved in a three-phonon scattering event. In its simple form Eq. (3.17) assumes that only the phonon mode $\boldsymbol{q}s$ is described by a displaced distribution and the other two modes obey the equilibrium distribution. Such a description is referred to as the *single-mode relaxation time* (*smrt*) approximation and can be justified to some extent [13]. Essentially, τ_{smrt} can be derived from the diagonal part of the phonon collision operator P. Modifications of the *smrt* has been proposed by Callaway [14] and Srivastava [15]. The validity of the relaxation-time approach is limited by the Landau–Peirls–Ziman condition [2]

$$\omega\tau > 1; \qquad \text{or} \quad \Lambda > \lambda, \tag{3.18}$$

where Λ and λ are phonon mean-free path and wavelength, respectively. Thus the Boltzmann-equation-based relaxation time approach is unsuitable for applications to samples thinner than average phonon wavelength.

Representing τ^* as the relaxation time for a chosen model (e.g. $\tau^* = \tau_{\text{smrt}} = \tau$ within the *smrt* approximation, or $\tau^* = \tau_C$ within the Callaway model), we can express the thermal conductivity tensor as

$$\kappa_{ij} = \frac{\hbar^2}{N_0 \Omega k_{\text{B}} T^2} \sum_{\boldsymbol{q}s} \omega^2(\boldsymbol{q}s) c_s^i(\boldsymbol{q}) c_s^j(\boldsymbol{q}) \tau^*(\boldsymbol{q}s) \bar{n}(\boldsymbol{q}s)(\bar{n}(\boldsymbol{q}s) + 1). \tag{3.19}$$

This expression will be discussed later using the *smrt* and Callaway models for the relaxation time.

3.3 Ingredients for Calculation of Thermal Conductivity

We will now consider calculation of lattice thermal conductivity using the relaxation-time-based expression in Eq. (3.19). It requires knowledge of (i) lattice dynamics, i.e. phonon dispersion curves ($\omega = \omega(\boldsymbol{q}s)$) and phonon density of states ($g(\omega)$), (ii) relaxation time $\tau_{\boldsymbol{q}s}$ for relevant phonon scattering processes, and (iii) an adequate procedure for carrying out summations over $\boldsymbol{q}$-vectors inside the Brillouin zone for the crystal structure under consideration.

3.3.1 Phonon Dispersion Curves and Density of States

The topic of lattice dynamics, fundamental to calculations of all properties related to atomic vibrations in solids, has been pursed for many decades. Both phenomenological and *ab initio* approaches have been employed. One of the most physically appealing phenomenological approaches for tetrahedrally bonded bulk semiconductors is the adiabatic bond charge model developed by Weber [16]. This method has been extended for application to surfaces [17] and nanostructured materials [18]. With the development of parameter-free total-energy calculations, *ab initio* methods of lattice dynamical calculations are now affordable (see, e.g., [19]). Details of such a method, based on the applications of the plane-wave pseudopotential technique, have been presented in the chapter by Tütüncü and Srivastava.

3.3.1.1 Bulk Materials

Figure 3.1 shows the phonon dispersion curves for bulk Si along the principal symmetry directions in the central primitive unit cell in momentum space (the Brillouin zone). Clearly, both the acoustic branches (characterised with $\omega = 0$ for $q = 0$) and optical branches (characterised with $\omega =$ constant for $q = 0$) are highly dispersive as well as anisotropic in the momentum space. In a vast majority of theoretical developments and numerical calculations of lattice thermal conductivity two major approximations are employed: (i) isotropic dispersion relations ($\omega(\boldsymbol{q}s) = \omega(|\boldsymbol{q}|s)$) and (ii) the continuum model ($\omega(qs) = c_s q$). Clearly, the continuum model is more suitable for low-frequency acoustic branches. In practice the isotropic continuum scheme is carried out inside a sphere (known as Debye sphere of radius q_{D}) as a replacement for the actual shape of the BZ. The volume of the Debye sphere should in principle be taken as the volume of the appropriate BZ. However, usually it is chosen to ensure that the integral of the density of states (DOS) equals the total number of acoustic modes. A comparison of the DOS, $g(\omega)$, results for Si obtained within the continuum approximation for an average acoustic branch (with average phase speed of 5,691 m/s) and the lattice dynamical dispersion relations is

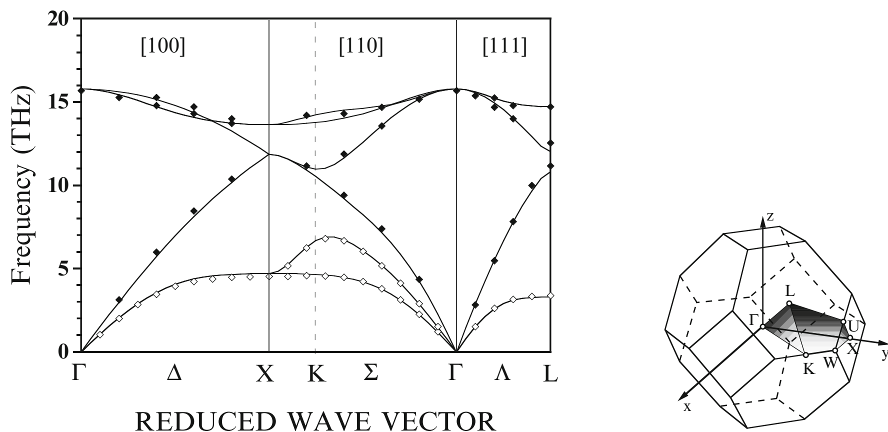

Fig. 3.1 Phonon dispersion curves for bulk Si. Theoretical results (*solid curves*) obtained from the application of the bond charge model compare well with experimentally measured results (*filled diamond* from [20] and *open diamond* from [21]). Also shown is the Brillouin zone and an irreducible part in it

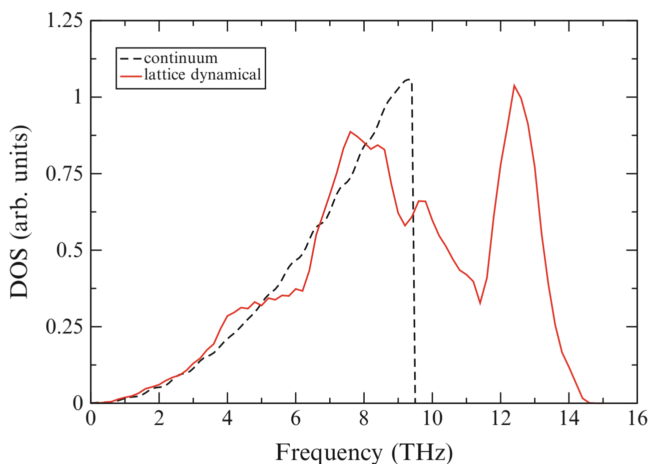

Fig. 3.2 Phonon density of states for bulk Si. The *solid curve* shows the results obtained from a full lattice dynamical calculation using the adiabatic bond charge model and the *dashed curve* is obtained from the consideration of the isotropic continuum model for an average acoustic branch

made in Fig. 3.2. The smooth quadratic rise of the continuum result, $g(\omega) \propto \omega^2$, is consistent with the realistic picture only in the low frequency range of 0–3.5 THz. Beyond this frequency range the realistic picture shows significant departure from the continuum results. In particular, the continuum model does not cover the optical frequency range and predicts a much larger DOS (a single van Hove singularity)

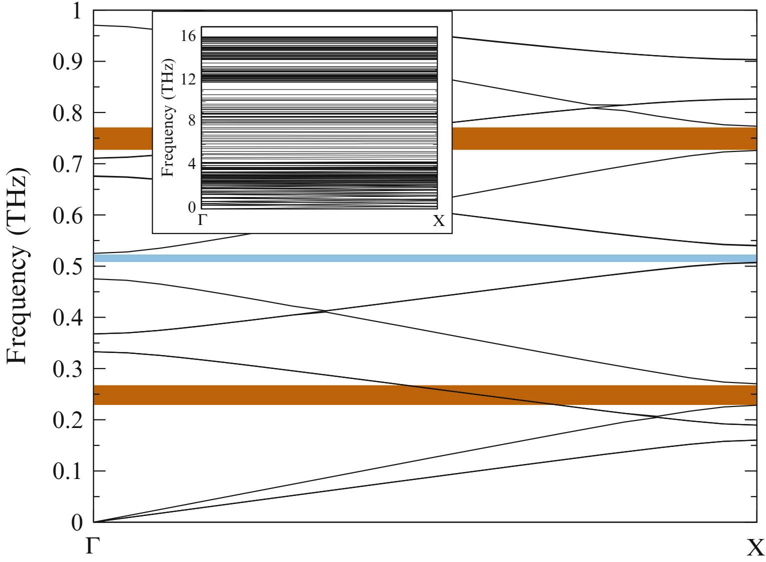

Fig. 3.3 Phonon dispersion curves for the Si(4 nm)/$Si_{0.4}Ge_{0.6}$(8 nm)[001] superlattice. The *inset* shows the full range of the spectrum. *Highlighted* are the lowest three LA gap regions. The *central gap region* is common to both LA and TA branches, indicating that the system is a true one-dimensional phononic along the grown direction. Taken from [18]

at the highest frequency (9.4 THz) modelled with the linear dispersion relation. In contrast, the realistic DOS shows several peaks (van Hove singularities), notably at frequencies 4, 7.6, 8.4, 9.7, and 12.5 THz.

3.3.1.2 Nanostructured Materials

Phonon dispersion curves of low-dimensional systems generally exhibit significant differences compared to bulk materials. There are at least three new features that can be expected to develop due to reduction in dimensionality: reduction in group velocity of phonons modes in all branches, creation of gaps in acoustic as well as optical branches both at zone edges and at zone centre, and confinement of higher lying acoustic and optical branches. We will explain these features by considering two examples: a thin Si/SiGe superlattice and ultrathin Si nanostructures.

Figure 3.3 shows the phonon dispersion curves, obtained from the application of an enhanced adiabatic bond charge model [18], for the Si(4 nm)/$Si_{0.4}Ge_{0.6}$(8 nm) superlattice along the growth direction [001]. This system exhibits several gaps in the phonon dispersion curves for the entire frequency range. Higher optical branches (with frequencies greater than 4 THz) show very flat dispersion curves (i.e. have low group velocities), indicating confinement effects within different superlattice layers. Several frequency gaps, for both longitudinal acoustic (LA) and transverse

acoustic (TA) branches, are obtained. The lowest three sub-terahertz LA gaps occur as follows: zone edge gap of 48 GHz centred 252 GHz, zone centre gap of 40 GHz centred 495 GHz, and zone edge gap of 30 GHz centred 805 GHz. These results are in good agreement with the sub-picosecond spectroscopic measurements made by Ezzahri et al. [22]. The lowest three TA gaps are: zone edge gap of 30 GHz centred 175 GHz, zone centre gap of 35 GHz centred 350 GHz, and zone edge gap of 33 GHz centred 523 GHz. The phonon speeds for the lowest TA and LA branches are 4.18 km/s and 6.00 km/s, respectively. These values are smaller than the average of the corresponding speeds in bulk Si and Ge. The theoretical work also shows that there is a clear overall gap along the superlattice growth direction between 515 and 539 GHz, meaning that this superlattice is a true one-dimensional phononic and would not allow propagation of phonons in this frequency range.

Figure 3.4 shows the phonon dispersion curves, obtained from the application of the adiabatic bond charge model, for ultrathin Si nanostructures such as a nanoslab, a wire, and a dot. Looking at the results for the nanoslab we note the existence of gap opening and flatness of branches along the slab normal (i.e. along $\Gamma - X$) compared to an in-plane direction. These features become even more prominent as the dimensionality decreases from two-dimensional (slab) to one-dimensional (wire) and zero-dimensional (dot). The confinement effect produces new peaks (van Hove singularities) in the phonon density of states (DOS). A clear example of this can be seen in the right-hand panel of Fig. 3.4b, which shows a comparison of the DOS of the Si nanowire of cross-section 0.543× 0.543 nm (solid curves) with that of bulk Si (dashed curves). In general, the nanowire DOS shows several sharp delta-like peaks, particularly at approximately 220 cm^{-1} where the bulk DOS shows a dip.

3.3.2 Brillouin Zone Summation

In order to obtain numerical values of any physical property of a crystalline material it is important to develop a method of Brillouin zone summation. Several methods exist for such an exercise, at different levels of sophistication. Let us consider the summation of a general periodic function $f(\boldsymbol{q})$

$$I = \sum_{\boldsymbol{q}} f(\omega(\boldsymbol{q})). \tag{3.20}$$

If the function $f(\omega(\boldsymbol{q}))$ is isotropic with a linear dispersion relation, i.e. $\omega(\boldsymbol{q}) = cq$, then the summation can be performed by using the Debye scheme. In this scheme the Brillouin zone summation is expressed as an integral over the Debye sphere of radius q_{D}

$$I = \int_0^{\omega_{\text{D}}} g_{\text{D}}(\omega) f(\omega) \text{d}\omega, \tag{3.21}$$

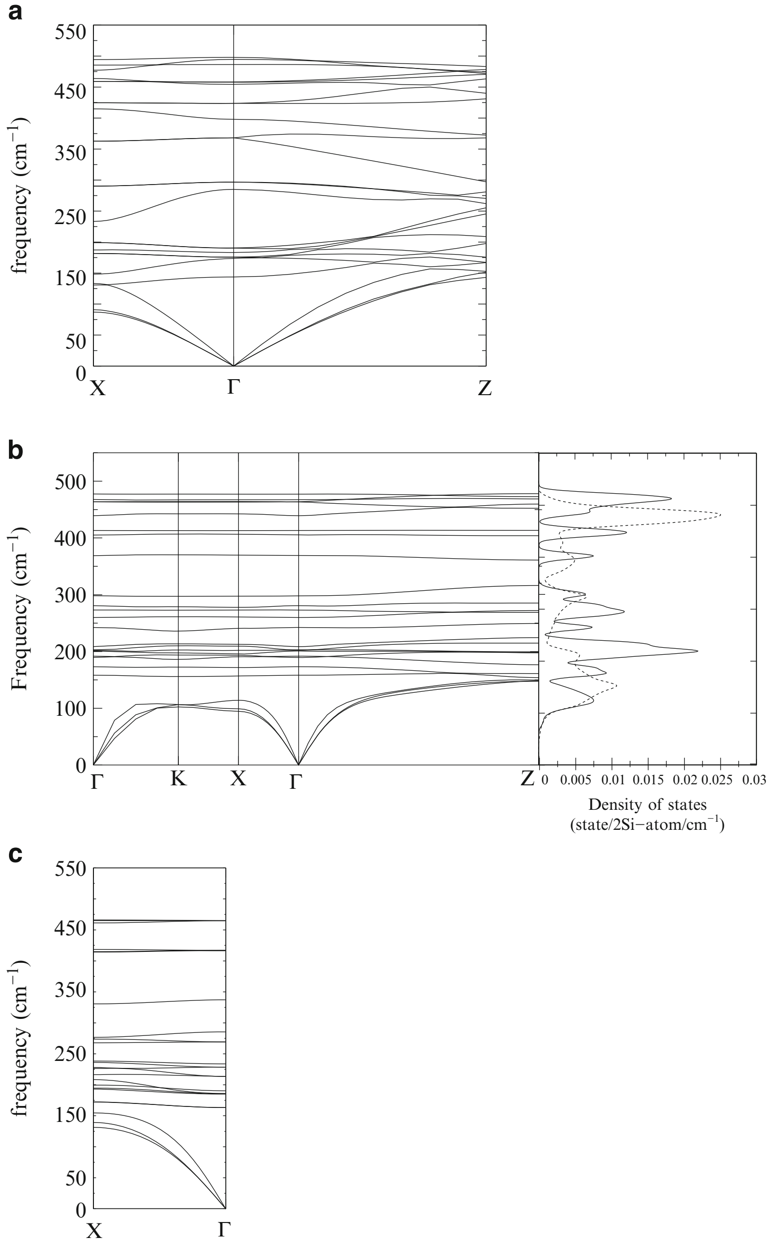

Fig. 3.4 Phonon dispersion curves for Si ultrathin nanostructures in the forms of: (**a**) nanoslab of thickness 0.543 nm, (**b**) rectangular nanowire of cross-section 0.543×0.543 nm, and (**c**) cubic nanodot of size 0.543×0.543×0.543 nm. $\Gamma - X$ is along the confinement direction. The *right-hand panel* in (**b**) shows a comparison of the density of states for the nanowire (*solid curves*) and bulk (*dashed curves*). Taken from [23]

where

$$g_{\mathrm{D}}(\omega) = \frac{N_0 \Omega}{2\pi^2} \frac{\omega^2}{c^3}, \tag{3.22}$$

is the Debye density of states function and $\omega_{\mathrm{D}} = c q_{\mathrm{D}}$ is the Debye frequency. The simple isotropic continuum Debye method must be improved adequately to deal with non-cubic crystal structures, and dispersive phonon modes in acoustic as well as optical branches.

A general-purpose scheme for numerical evaluation of an integral of the type in Eq. (3.20) is based on the concept of "special $\boldsymbol{q}$-points" [24, 25] inside the Brillouin zone for the crystal under consideration. Considering an appropriate selection of N special $\{\boldsymbol{q}_i\}$ points and weight factors $\{W(\boldsymbol{q}_i)\}$ associated with them, we can estimate the integral I as

$$I \simeq N_0 \sum_i^N f(\omega(\boldsymbol{q}_i)) W(\boldsymbol{q}_i). \tag{3.23}$$

For a given shape of Brillouin zone, different sets of special $\{\boldsymbol{q}_i\}$ points can be generated. A set is considered more "efficient" if it provides an acceptable result for the integral with the least number of $\{\boldsymbol{q}_i\}$ points [24].

3.3.3 Phonon Scattering Processes

Expressions for phonon scattering rates from various sources in bulk semiconductors can be derived by applying Fermi's Golden rule formula based on first-order time-dependent perturbation theory, and do exist in the literature (see, e.g. [3] and references therein). Here we simply reproduce some of the commonly used results.

3.3.3.1 Boundary Scattering

Purely diffusive phonon scattering rate from crystal boundaries can be expressed as

$$\tau_{\mathrm{bs}}^{-1}(\boldsymbol{q}s) = c_s / L_0. \tag{3.24}$$

Here L_0 denotes an effective boundary length, which depends on the geometrical shape of crystal. $L_0 = D$ for a crystal of cylindrical shape with circular cross-section of diameter D, and $L_0 = 1.12\ d$ for a square cross-section of side d. For polycrystalline solids L_0 is a measure of an effective grain size.

In reality, consideration of the *polish* quality of crystal surface must be made and an effective boundary length determined. This can be quite a difficult task,

knowing especially that the precise nature of surface roughness and structure of grown samples is usually ill-defined. A phenomenological model [2] allows us to define an effectively longer boundary length L by incorporating the surface *polish* quality in terms of the *specularity* factor p,

$$L = \frac{(1+p)}{(1-p)} L_0. \tag{3.25}$$

The limiting cases $p = 0$ and $p = 1$ are purely diffusive (or Casimir) scattering and purely specular boundary scattering (or reflection), respectively. For a given p factor, each phonon is reflected $1/(1-p)$ times before being diffusively scattered.

3.3.3.2 Isotopic Mass-Defect Scattering

Consider a crystal with an average mass per unit cell as $\bar{M}$ and let f_i be the fraction of the unit cell containing the isotopic mass M_i. The scattering rate of a phonon mode $\boldsymbol{q}s$ due to isotopic mass defects is [3, 13]

$$\tau_{\mathrm{md}}^{-1}(\boldsymbol{q}s) = \frac{\Gamma_{\mathrm{md}}\pi}{6N_0}\omega^2(\boldsymbol{q}s)g(\omega(\boldsymbol{q}s)), \tag{3.26}$$

where $g(\omega)$ is the density of states and Γ_{md} is the isotopic mass parameter. Within the isotropic continuum approximation, the expression in Eq. (3.26) reads

$$\begin{aligned} \tau_{\mathrm{md}}^{-1}(\boldsymbol{q}s) &= \frac{\Gamma_{\mathrm{md}}\Omega}{4\pi\bar{c}^3}\omega^4(\boldsymbol{q}s), \\ &= A_{\mathrm{md}}\omega^4(\boldsymbol{q}s), \end{aligned} \tag{3.27}$$

with $\bar{c}$ as the average acoustic phonon speed. For a single-species crystal the isotopic mass parameter is evaluated as

$$\Gamma_{\mathrm{md}} = \sum_i f_i(\Delta M_i/\bar{M})^2, \tag{3.28}$$

with $\Delta M_i = M_i - \bar{M}$, and M as the mass of atoms in the unit cell of volume Ω. Clearly, for a monatomic crystal, with one atom per unit cell, M is the mass of a single atom and Ω represents the atomic volume. For a composite material with molecular formula $A_xB_yC_z\ldots$ we can express Γ_{md} as [26]

$$\begin{aligned} \Gamma_{\mathrm{md}} = &\frac{x}{(x+y+z+\ldots)}\left(\frac{M_A}{\bar{M}}\right)^2\Gamma(A) \\ &+\frac{y}{(x+y+z+\ldots)}\left(\frac{M_B}{\bar{M}}\right)^2\Gamma(B) \end{aligned}$$

$$+\frac{z}{(x+y+z+\dots)}\left(\frac{M_C}{\bar{M}}\right)^2\Gamma(C)$$
$$+\dots, \tag{3.29}$$

with

$$\Gamma(A)=\sum_i f_i\left(\frac{\Delta M_i(A)}{\bar{M}_A}\right)^2, \tag{3.30}$$

etc. and

$$\bar{M}=\frac{xM_A+yM_B+zM_C+\dots}{x+y+z+\dots}. \tag{3.31}$$

The above expression can be used for a superlattice structure $(AB)_n(CD)_m$ by considering it as a compound with formula $A_nB_nC_mD_m$.

3.3.3.3 Interface Scatterings

Low-dimensional solids, such as superlattices, and nanowires or nanodots embedded in a host matrix, can provide additional defect-related phonon scattering mechanisms: interface mass-mixing scattering (IMS) due to diffusion or mixing of atoms across interfaces, and interface dislocation scattering (IDS) which results from dislocations or missing bonds present at interfaces. The IMS scattering rate from a periodic distribution of nanodots in a host matrix has been studied by treating the embedded material as a small perturbation to the host material [27,28]. Here we briefly discuss the IMS for superlattice structures with planar (two-dimensional) interfaces [29].

(i) Mass-mixing scattering:

Let us consider a periodic un-reconstructed superlattice A_m/B_n with N_0 unit cells, and each unit cell containing m atomic layers of material A and n layers of material B. Assuming that interface mass mixing takes place within J layers on either side of an interface, for dealing with the theory of IMS the perturbed crystal Hamiltonian can be expressed as

$$H'(\mathrm{IMS})=\frac{1}{2}\sum_{i=m-J}^{m}(M_i|\mathbf{v_i}|^2-M_A|\mathbf{v_A}|^2)+\frac{1}{2}\sum_{i=m+1}^{m+J}(M_i|\mathbf{v_i}|^2-M_B|\mathbf{v_B}|^2). \tag{3.32}$$

where M_i is the mass of the ith atom, and $\mathbf{v}_i=\mathrm{d}\mathbf{u_i}/\mathrm{d}t$ with $\mathbf{u_i}$ being the relative displacement of the ith with respect to its neighbours. Application of Fermi's golden rule and utilisation of some simplifying assumptions lead to the following expression for the relaxation of a phonon mode $\boldsymbol{q}s$ [29]

$$\tau_{\rm IMS}^{-1}(\mathbf{q}s) = \frac{\alpha\pi}{2N_0(n+m)^2}\int d\omega(\boldsymbol{q}'s')g(\omega(\boldsymbol{q}'s'))\omega(\boldsymbol{q}s)\omega(\boldsymbol{q}'s')$$
$$\times\frac{\bar{n}(\boldsymbol{q}'s')+1}{\bar{n}(\boldsymbol{q}s)+1}\delta(\omega(\boldsymbol{q}s)-\omega(\boldsymbol{q}'s')\left[\left(1-\frac{e_A e'_A}{e_B e'_B}\right)^2+\left(1-\frac{e_B e'_B}{e_A e'_A}\right)^2\right], \tag{3.33}$$

where α is regarded as a parameter related to the amount of mixing at the interface, $g(\omega(\boldsymbol{q}s))$ is the density of states, and e_B/e_A is the ratio of the amplitudes of eigenvectors in materials B and A along the superlattice growth direction.

(ii) Interface dislocation scattering:

Superlattices composed of lattice-mismatched layers are known to be characterised by the presence of dislocations at interfaces. Phonon scattering rate by such dislocations cannot adequately be described by the traditional theory for bulk solids. While the phonon scattering rate by dislocations in bulk has traditionally been derived by treating solids as elastic continuum (see, e.g., [2]), an atomic-scale theory is required when dealing with scattering from interface dislocations. Let us consider an interface dislocation as a series of randomly missing bonds located near the interface within a unit cell. With such a consideration we can write the perturbed crystal Hamiltonian as

$$H'(\mathrm{IDS})=\frac{1}{2}\sum_{i=m-I}^{m}(K_0|\boldsymbol{u}_i|^2-K_A|\boldsymbol{u}_A|^2)+\frac{1}{2}\sum_{i=m+1}^{m+I}(K_0|\boldsymbol{u}_i|^2-K_B|\boldsymbol{u}_B|^2), \tag{3.34}$$

where u_i as the relative displacement between two neighbouring atoms and I is number of atomic layers with broken bonds on either side of an interface, $K_A(K_B)$ represents the inter-atomic spring constant in the layer A(B), and K_0 represents a spring constant in the dislocation region, i.e. has a value equal or close to zero, for broken or missing bonds. From the application of Fermi's golden rule the following expression can be derived for phonon-IDS relaxation rate [29]

$$\tau_{\rm IDS}^{-1}(\boldsymbol{q}s) = \frac{\pi\omega_0^4}{4N_0}\frac{\alpha'}{(n+m)^2}\int d\omega(\boldsymbol{q}'s')\frac{g(\omega(\boldsymbol{q}'s'))}{\omega(\boldsymbol{q}s)\omega(\boldsymbol{q}'s')}\frac{\bar{n}(\boldsymbol{q}'s')+1}{\bar{n}(\boldsymbol{q}s)+1}$$
$$\times\delta(\omega(\boldsymbol{q}s)-\omega(\boldsymbol{q}'s'))\left[1+\left(\frac{e_A e'_A}{e_B e'_B}\right)^2+1+\left(\frac{e_B e'_B}{e_A e'_A}\right)^2\right], \tag{3.35}$$

where α' is a measure of dislocation concentration and ω_0 can be approximated as the highest zone-centre frequency.

The following simplified expression for the amplitude ratio e_B/e_A, required for both IMS and IDS, can be derived by treating a superlattice as a diatomic linear chain along the growth direction

$$\frac{e_B}{e_A} = \frac{\left[\frac{1}{M_0} - \Delta\left(\frac{1}{M}\right)\right]\cos(l_z q_z)}{\left[\left(\frac{1}{M_0}\right)^2 \cos^2(l_z q_z) + \left(\Delta\left(\frac{1}{M}\right)\right)^2 \sin^2(l_z q_z)\right]^{\frac{1}{2}} - \Delta\left(\frac{1}{M}\right)}, \tag{3.36}$$

where $2M_0 = 1/M_A + 1/M_B$, and $\Delta(1/M) = (1/M_A - 1/M_B)/2$, and l_z is the superlattice period.

3.3.3.4 Anharmonic Scattering

Anharmonic interatomic potential is present in all crystals at finite temperatures. Obtaining an expression for crystal anharmonic potential, with its temperature dependence, from first principles is an enormous task and has not yet been achieved satisfactorily. A workable form of cubic anharmonic crystal potential can be expressed, by treating a crystal as an isotropic anharmonic elastic continuum, as [2, 3]

$$V_3 = \frac{1}{3!}\sqrt{\frac{\hbar^3}{2\rho \mathrm{N}_0 \Omega}}\frac{\gamma(T)}{\bar{c}} \sum_{\boldsymbol{q}s\boldsymbol{q}'s'\boldsymbol{q}''s''} \sqrt{\omega(\boldsymbol{q}s)\,\omega(\boldsymbol{q}'s')\,\omega(\boldsymbol{q}''s'')}$$

$$\times(a^{\dagger}_{\boldsymbol{q}s} - a_{-\boldsymbol{q}s})(a^{\dagger}_{\boldsymbol{q}'s'} - a_{-\boldsymbol{q}'s'})(a^{\dagger}_{\boldsymbol{q}''s''} - a_{-\boldsymbol{q}''s''})\,\delta_{\boldsymbol{q}+\boldsymbol{q}'+\boldsymbol{q}'',\mathbf{G}}, \tag{3.37}$$

where $\gamma(T)$ as a mode-average but temperature-dependent Grüneisen's constant, $\mathbf{G}$ is a reciprocal lattice vector, and $a^{\dagger}_{\boldsymbol{q}s}$, $a_{\boldsymbol{q}s}$, etc. are the phonon creation and annihilation operators, respectively, and other symbols have previously been defined. It should be remarked that the above form of the anharmonic potential assumes that the phonon spectrum consists of only acoustic branches. Recently, a form of isotropic elastic anharmonic potential has been modelled [30] that considers acoustic as well as optical phonon branches. Here we will, however, neither present that form of the Hamiltonian nor any results obtained from its applications.

Application of Fermi's golden rule leads to the following single-mode relaxation time for a phonon mode $\boldsymbol{q}s$ due to the anharmonic three-phonon interactions in a bulk single crystal (see [3] for details):

$$\tau^{-1}(\boldsymbol{q}s)\,|_{\text{bulk}} = \frac{\pi\hbar\rho^2\gamma^2}{N_0\Omega\bar{c}^2} \sum_{\boldsymbol{q}'s',\boldsymbol{q}''s'',\boldsymbol{G}} B(\boldsymbol{q}s, \boldsymbol{q}'s', \boldsymbol{q}''s''), \tag{3.38}$$

with

$$B(\mathbf{q}s, \mathbf{q}'s', \mathbf{q}''s'') = \omega(\mathbf{q}s)\omega(\mathbf{q}'s')\omega(\mathbf{q}''s'')\bar{n}(\mathbf{q}'s')$$
$$\times\left\{\left[\frac{(\bar{n}(\mathbf{q}''s'')+1)}{\bar{n}(\mathbf{q}s)+1}\delta(\omega(\mathbf{q}s)+\omega(\mathbf{q}'s')-\omega(\mathbf{q}''s''))\delta_{\mathbf{q}+\mathbf{q}',\mathbf{q}''+\mathbf{G}}\right]\right.$$
$$\left.+\left[\frac{1}{2}\frac{\bar{n}(\mathbf{q}''s'')}{\bar{n}(\mathbf{q}s)}\delta(\omega(\mathbf{q}s)-\omega(\mathbf{q}'s')-\omega(\mathbf{q}''s''))\delta_{\mathbf{q}+\mathbf{G},\mathbf{q}'+\mathbf{q}''}\right]\right\} \tag{3.39}$$

The processes described by the first and second terms in Eq. (3.39) may be referred to as Class 1 and Class 2 events, governed by the momentum and energy conservation conditions:

$$\text{Class 1 events}: \quad \mathbf{q}+\mathbf{q}' = \mathbf{q}''+\mathbf{G}; \quad \omega+\omega' = \omega'', \tag{3.40}$$

$$\text{Class 2 events}: \quad \mathbf{q}+\mathbf{G} = \mathbf{q}'+\mathbf{q}''; \quad \omega = \omega'+\omega''. \tag{3.41}$$

For each class, an event is called Normal (N) if it involves wavevectors of all participating phonons within the central Brillouin zone. If a reciprocal lattice vector $\mathbf{G}$ is required to meet the momentum conservation condition, the event is called Umklapp (U). These processes are schematically illustrated for a class 1 event in panels (a) and (b) of Fig. 3.5.

Callaway [14] took into account the momentum conserving condition of N-processes to derive an effective phonon relaxation time τ_C, which can be considered as a modification of the single-mode relaxation time τ_{smrt}. Within the isotropic continuum approximation, the following expression can be derived [31]

$$\tau_C = \tau_{\text{smrt}}(1+\beta/\tau_N), \tag{3.42}$$

with τ_N as the relaxation time due to N processes, and

$$\beta = \frac{q}{\omega(\mathbf{q}s)c_s(\mathbf{q})}\frac{\langle \omega c q \tau \tau_N{}^{-1}\rangle}{\langle q^2\tau_N{}^{-1}(1-\tau\tau_N{}^{-1})\rangle}, \tag{3.43}$$

where the following notation has been used

$$< f >= \sum_{\mathbf{q}s} f(\mathbf{q}s)\bar{n}(\mathbf{q}s)(\bar{n}(\mathbf{q}s)+1). \tag{3.44}$$

The above theory can be adopted for low-dimensional systems, but with modifications. Let us consider a superlattice structure as an example. Apart from making the obvious changes in the material density (ρ_{sl}), Grüneisen's constant (γ_{sl}) and average acoustic phonon speed ($\bar{c}_{\text{sl}}$), two further considerations must be made. (i) The shortest reciprocal lattice vector in the superlattice growth direction will in

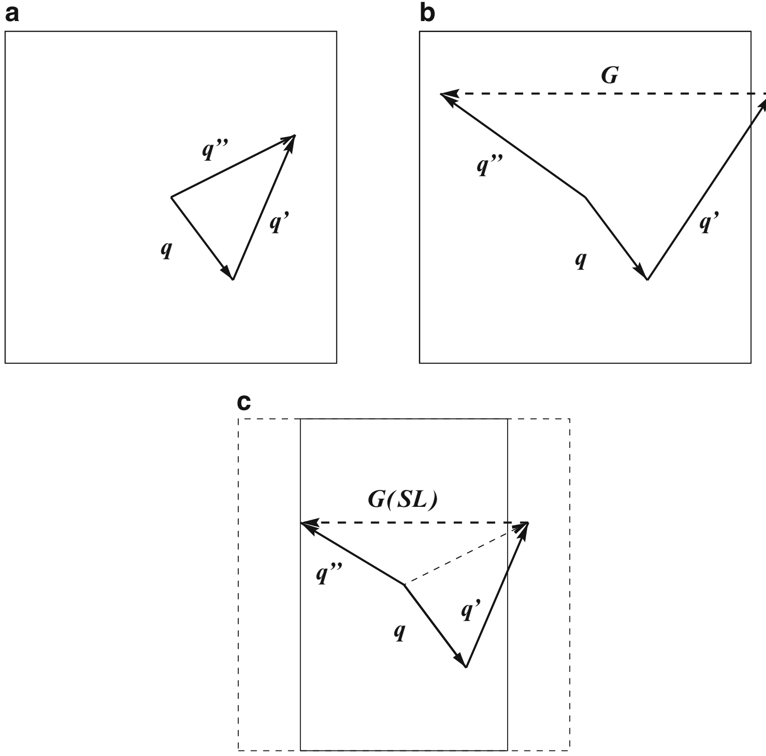

Fig. 3.5 Schematic illustration of a Class 1 three-phonon scattering process in a single-crystal solid: (**a**) an N process and (**b**) an U process. (**c**) shows how the bulk N process shown in (**a**) becomes a "mini-U" process in a superlattice structure corresponding to a superlattice reciprocal lattice vector $\boldsymbol{G}$(SL). For clarity, in (**c**) the bulk Brillouin zone is drawn by *dashed lines*, and the bulk $\boldsymbol{q}''$ is shown by the *short-dashed vector*

general be much shorter than the shortest reciprocal lattice vector in the constituent materials. A simple illustration is provided in panel (c) of Fig. 3.5. This means that some of the bulk N-processes will turn into the superlattice mini-U processes. (ii) The presence of two materials in an A/B superlattice structure has to be incorporated in deriving an appropriate form of the anharmonic crystal potential V_3. An attempt in this regard was made by Ren and Dow [32]. Using a scheme similar to Ren and Dow, a suitable modification of the expression in Eq. (3.38) for an A/B superlattice structure can be presented as

$$\tau^{-1}(\boldsymbol{q}s)\mid_{\text{superlattice}} = \frac{\pi\hbar\rho_{\text{sl}}^2\gamma_{\text{sl}}^2}{N_0\Omega\bar{c}_{\text{sl}}^2}\sum_{\boldsymbol{q}'s',\boldsymbol{q}''s'',\boldsymbol{G}_{\text{sl}}} B(\boldsymbol{q}s,\boldsymbol{q}'s',\boldsymbol{q}''s'')F_{\text{sl}}(\boldsymbol{q}s,\boldsymbol{q}'s',\boldsymbol{q}''s''), \tag{3.45}$$

where ρ_{sl} is superlattice density (i.e. the weighted average density of the two materials), $\bar{c}_{\text{sl}}$ is the average acoustic velocity in the superlattice, γ_{sl} is the Grüneisen

constant for the joint system, $\boldsymbol{G}_{\rm sl}$ represents a reciprocal lattice vector for the superlattice structure, and the term $F_{\rm sl}$ arises due to the presence of two materials in the system. Within the diatomic linear chain approximation, the term $F_{\rm sl}$ can be expressed as

$$F_{\rm sl}(\boldsymbol{q}s,\boldsymbol{q}'s',\boldsymbol{q}''s'')=\frac{1}{64}\left\{\frac{1}{2\rho_A^{\frac{3}{2}}}\left[1+\frac{\rho_A^{\frac{1}{2}}}{\rho_B^{\frac{1}{2}}}\left(\frac{e_B}{e_A}+\frac{e'_B}{e'_A}+\frac{e''_B}{e''_A}\right)+\frac{\rho_A}{\rho_B}\left(\frac{e_Be'_B}{e_Ae'_A}+\frac{e'_Be''_B}{e'_Ae''_A}+\frac{e_Be''_B}{e_Ae''_A}\right)\right.\right.$$
$$\left.+\frac{\rho_A^{\frac{3}{2}}}{\rho_B^{\frac{3}{2}}}\left(\frac{e_Be'_Be''_B}{e_Ae'_Ae''_A}\right)\right]+\frac{1}{2\rho_B^{\frac{3}{2}}}\left[1+\frac{\rho_B^{\frac{1}{2}}}{\rho_A^{\frac{1}{2}}}\left(\frac{e_A}{e_B}+\frac{e'_A}{e'_B}+\frac{e''_A}{e''_B}\right)+\frac{\rho_B}{\rho_A}\left(\frac{e_Ae'_A}{e_Be'_B}+\frac{e'_Ae''_A}{e'_Be''_B}+\frac{e_Ae''_A}{e_Be''_B}\right)\right.$$
$$\left.\left.+\frac{\rho_B^{\frac{3}{2}}}{\rho_A^{\frac{3}{2}}}\left(\frac{e_Ae'_Ae''_A}{e_Be'_Be''_B}\right)\right]\right\}^2, \tag{3.46}$$

where $e'_A \equiv e_A(\boldsymbol{q}'s')$, $e''_A \equiv e''_A(\boldsymbol{q}''s'')$, etc., ρ_A and ρ_B are the densities of materials A and B, respectively, and the expression for amplitude ratio e_B/e_A is given in Eq. (3.36).

3.3.3.5 Scattering from Donor Electrons

We will consider the scattering of phonons with donor electrons in doped semiconductors. In a doped semiconductor we may consider a local displacement field $\boldsymbol{u}(\mathrm{r})$ produced by longitudinal acoustic phonons, causing an energy change of the form $E_d = C\Delta(\boldsymbol{r}) = C_1\nabla\cdot\boldsymbol{u}(\mathrm{r}) = C_2\hat{\boldsymbol{q}}\cdot\boldsymbol{e}_{\boldsymbol{q}s}$, with C_1 and C_2 as some parameters. The matrix element of the deformation potential E_d can be evaluated by expressing the donor electron wave function as a Bloch function. Application of Fermi's golden rule results in the following expression for the relaxation rate of a phonon mode $\boldsymbol{q}s$ (see [33, 34] for details)

$$\tau^{-1}(\boldsymbol{q}s) = \frac{m^{\star 2}E_d^2k_{\rm B}T}{2\pi\rho c_{\rm L}\hbar^4}\left[z-\ln\left(\frac{1+\exp(\xi-\xi_0+z^2/16\xi+z/2)}{1+\exp(\xi-\xi_0+z^2/16\xi-z/2)}\right)\right], \tag{3.47}$$

with $c_{\rm L}$ is the speed of longitudinal acoustic phonons, $z = \hbar\omega/k_{\rm B}T$, $\xi = m^\star c_{\rm L}^2/2k_{\rm B}T$ and $\xi_0 = \zeta/k_{\rm B}T$. This expression can be reduced to the following form in the case of a heavily doped, degenerate, semiconductor with $\zeta > E_0$ and $\zeta - E_0 >> k_{\rm B}T$, where $E_0 = \hbar^2\omega^2/8m^\star c_{\rm L}^2 + \frac{1}{2}m^\star c_{\rm L}^2 - \hbar\omega/2$,

$$\tau^{-1}(\boldsymbol{q}s) = \frac{m^{\star 2}E_d^2}{2\pi\rho\hbar^3c_{\rm L}}\omega. \tag{3.48}$$

For moderately doped semiconductors, Eq. (3.47) can be reduced to the following form [35]

$$\tau^{-1}(\boldsymbol{q}s) = \frac{n_c E_d^2 \omega}{\rho c_L^2 k_B T} \sqrt{\frac{\pi m^* c_L^2}{2k_B T}} \exp\left(\frac{-m^* c_L^2}{2k_B T}\right), \tag{3.49}$$

where n_c is the carrier concentration.

3.4 Thermal Conductivity Results

Numerical calculations of thermal properties, such as lattice specific heat and lattice thermal conductivity (κ), require summation, or integration, of functions of phonon wave vectors over the entire Brillouin zone (BZ). In Sect. 3.3.2 we have mentioned two approaches for carrying out BZ summation. In this section we will present results of numerical calculations of κ for bulk and low-dimensional semiconductors. Some of the results have been obtained by using Debye's isotropic continuum method. Some other results have been carried out by using full lattice dynamical results for phonon dispersion curves, phonon velocities, and a realistic BZ summation technique.

Traditionally calculations of thermal properties have been carried out within Debye's isotropic continuum scheme. Within this scheme Callaway's expression for the lattice thermal conductivity can be written as follows:

$$\begin{aligned} \kappa_C &= \frac{\hbar^2 q_D^5}{6\pi^2 k_B T^2} \\ &\quad \times \Big[\sum_s c_s^4 \int_0^1 \mathrm{d}x x^4 \tau \bar{n}(\bar{n}+1) + \frac{\{\sum_s c_s^2 \int_0^1 \mathrm{d}x x^4 \tau \tau_N^{-1} \bar{n}(\bar{n}+1)\}^2}{\sum_s \int_0^1 \mathrm{d}x x^4 \tau_N^{-1}(1-\tau\tau_N^{-1})\bar{n}(\bar{n}+1)} \Big], \\ &= \kappa_D + \kappa_{N-\text{drift}}, \end{aligned} \tag{3.50}$$

where $x = q/q_D$ with q_D representing the Debye radius. The first and second terms in the above equation represent the single-mode relaxation time result κ_{smrt} (the Debye term κ_D) and the N-drift term $\kappa_{N-\text{drift}}$, respectively. The total phonon relaxation time is the sum of contributions to τ^{-1}, obtained within the isotropic continuum scheme, from all scattering processes relevant to the system under study. Expressions for commonly required processes are given in Sect. 3.3.3. Using the anharmonic crystal potential presented in Sect. 3.3.3.4 and employing Debye's isotropic continuum scheme, the anharmonic phonon relaxation time contributed by three-phonon processes can be expressed as follows (see [3] for details):

$$\tau_{qs}^{-1}(3\text{ ph}) = \frac{\hbar q_{\mathrm{D}}^5 \gamma^2}{4\pi\rho\bar{c}^2} \sum_{s's''\epsilon} c_s c_{s'}$$

$$\Big[\int dx' x'^2 x''_+ \{1-\epsilon+\epsilon(Cx+Dx')\} \frac{\bar{n}_{q's'}(\bar{n}''_+ + 1)}{(\bar{n}_{qs}+1)}$$

$$+\frac{1}{2}\int \mathrm{d}x' x'^2 x''_- \{1-\epsilon+\epsilon(Cx-Dx')\} \frac{\bar{n}_{q's'}\bar{n}''_-}{\bar{n}_{qs}} \Big].$$

Here $x' = q'/q_{\mathrm{D}}$, $x''_\pm = Cx \pm Dx'$ and $\bar{n}''_\pm = \bar{n}(x''_\pm)$, $C = c_s/c_{s''}$, $D = c_{s'}/c_{s''}$, $\epsilon = 1$ for momentum conserving (normal, or N) processes, and $\epsilon = -1$ for momentum non-conserving (Umklapp, or U) processes. The first and second terms in the above equation are contributed by class 1 events $\boldsymbol{q}s + \boldsymbol{q}'s' \rightarrow \boldsymbol{q}''s''$ and class 2 events $\boldsymbol{q}s \rightarrow \boldsymbol{q}'s' + \boldsymbol{q}''s''$, respectively. The integration limits on the variable x', imposed by the energy and momentum conservation conditions in Eqs. (3.40) and (3.41), can be derived straightforwardly and are given below.

Class 1 events:

$$0 \le x \le 1$$

$$0, \frac{(1-C)x}{(1+D)} \le x' \le \frac{(1+C)x}{(1-D)}, \frac{(1-Cx)}{D}, 1 \qquad N \text{ processes},$$

$$0, \frac{(2-(1+C)x)}{(1+D)} \le x' \le \frac{(1-Cx)}{D}, 1 \qquad U \text{ processes}. \tag{3.51}$$

Class 2 events:
N processes:

$$0 \le x \le 1$$

$$0, \frac{(C-1)x}{D+1}, \frac{(Cx-1)}{D} \le x' \le \frac{(C+1)x}{D+1}, \frac{(C-1)x}{D-1}, 1 \tag{3.52}$$

U processes:

$$\frac{2}{1+C} \le x \le 1$$

$$0, \frac{2-(1+C)x}{1-D}, \frac{Cx-1}{D}, \frac{(C+1)x-2}{D+1} \le x' \le \frac{(C+1)x-2}{D-1}, 1. \tag{3.53}$$

3.4.1 Bulk Semiconductors

Figure 3.6 shows the temperature variation of the lattice thermal conductivity of bulk Si, Ge, and GaAs. The theory employed for numerical calculations was based on the

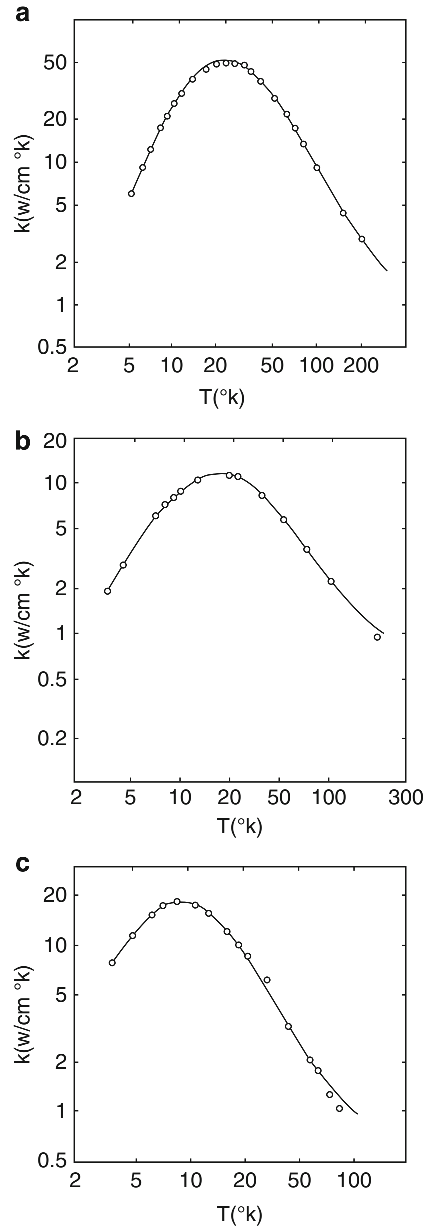

Fig. 3.6 Thermal conductivity results for bulk semiconductors: (**a**) Si, (**b**) natural Ge, and (**c**) GaAs. *Solid curves* are obtained from theoretical calculations. *Symbols* represent experimentally measured values: Si [36]; Ge (natural sample of Geballe and Hull [37]); GaAs [26]. Reproduced from Srivastava [38]

Srivastava's model [15] for an effective phonon relaxation time, *viz.* a modified form of Callaway's model [14]. The numerical results, obtained by employing Debye's isotropic continuum method and using reasonable values of fitting parameters, agree well with experimentally measured results. In general, with increase in

temperature, κ increases as T^3 at low temperatures when the phonon-boundary scattering dominates, reaches a maximum in the temperature range 10–30 K due to the combined effect of defect and anharmonic scatterings of phonons, and decreases as $1/T$ at high temperatures when three-phonon scattering processes dominate. The maximum value of κ is generally determined by the average atomic mass and the level of sample purity. The maximum value of κ is approximately 5,000, 1,300, and 2,500 W/m-K and occurs at approximately 20, 20, and 15 K for Si, natural Ge, and GaAs, respectively. The room temperature values of κ are 130, 58, and 55 W/m-K for Si, Ge, and GaAs, respectively. Of these three semiconductors, Si is categorised as a "high thermal conductivity material" (a material with room-temperature conductivity larger than 100 W/m-K).

3.4.2 GaAs Suspended Nanobeams

Fon et al. [39] fabricated suspended GaAs nanobeams and made the first direct measurement of the thermal conductance in such structures. They considered a total of four samples: undoped nanobeam, doped nanobeam, a 6-beam device (4 doped nanobeams and 2 undoped nanobeams), and a 4-beam device (4 doped nanobeams). The nanobeams were of rectangular shape with cross-sectional dimensions d_1 = 100 nm and d_2 = 250 nm. Results for bulk and the four nanobeams of GaAs, obtained from numerical evaluation of the conductivity expression in Eq. (3.50) and the phonon anharmonic relaxation time expression in Eq. (3.51), are presented in Fig. 3.7. The parameters used in the calculations for bulk, undoped nanobeam, doped nanobeam, 6-beam device, and 4-beam device, respectively, were: 0.73 cm, 0.227 μm, 0.21 μm, 0.50 μm, and 0.37 μm for the effective boundary length; 0.0, 0.5, 0.4, 0.5, and 0.4 for the surface specularity parameter p; 0.0, 0.0, 5.0×10^{24} m^{-3}, 0.0, and 5.0×10^{24} m^{-3} for the donor electron concentration; 4.36×10^{-42} s^3, 46.76×10^{-42} s^3, 436.27×10^{-42} s^3, 31.2×10^{-42} s^3, and 311.7×10^{-42} s^3 for the mass defect parameter A_{md} in Eq. (3.27). The Grüneisen constant was set to 1.8 for all the samples. We will describe the role of various phonon scattering processes in explaining the experimental results for bulk GaAs [26] and the nanobeam structures [39] in the following paragraphs.

In bulk GaAs, phonon boundary scattering is only important below 10 K. In contrast, boundary scattering has a very strong influence on the thermal conductivity of the undoped nanobeam up to about 100 K, and it also controls the shape of the thermal conductivity curve up to about 300 K. In order to explain the low-temperature conductivity results of the nanobeams it was necessary to include specular phonon boundary scattering events. Our fitted value of the effective boundary length of 0.68 μm is consistent with the specularity factor $p = 0.5$. This suggests that each phonon is specularly reflected on an average of $1/(1 - p) \approx 2$ times before being diffusely scattered in these nanobeams. Our work also suggests that, compared to bulk, phonon scattering by point defects is much stronger

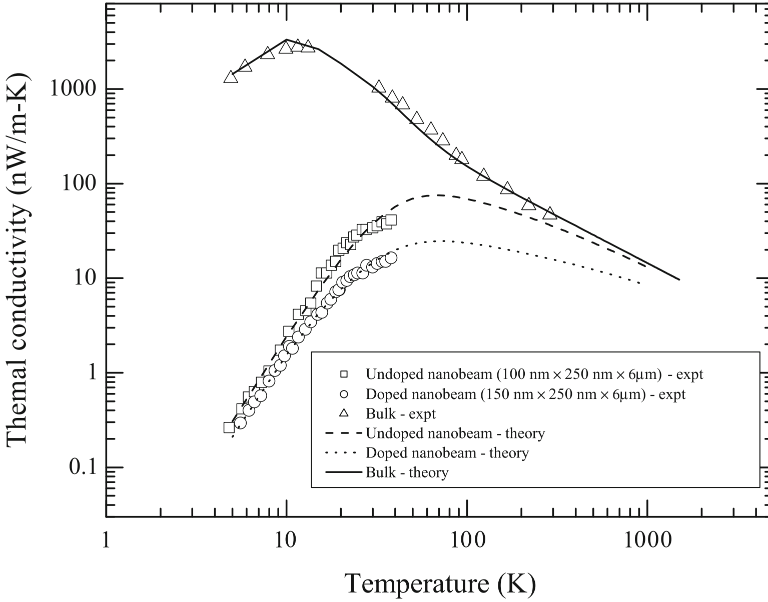

Fig. 3.7 Thermal conductivity of bulk GaAs (theory: *solid curve*; experiment [26]: *triangles*). Also shown are the thermal conductivity results for suspended GaAs nanobeams (theory: *dotted curves*; experiment [39]: *squares and circles*). Reproduced from [40]

in the nanobeams. The fitted values of the effective boundary length are much larger than the effective physical width $L_0 = 1.12\sqrt{d_1 d_2} = 0.177$ μm of the nanobeams fabricated by Fon et al. A similar conclusion was reached by Fon et al. in their attempt to theoretically explain the low-temperature conductivity results. Surprisingly, in our theoretical work we had to use a big range of effective boundary length (from 0.49 μm for doped beam to 1.5 μm for the six-beam device).

The doped beams fabricated by Fong et al. contain donor dopants with concentration 5×10^{18} cm^{-3} in the topmost 50 nm layers. We used Eq. (3.49) to account for the electron–phonon scattering in this sample. However, in order to successfully explain the conductivity results of the doped nanobeams, we had to consider the point defect scattering rate approximately 10 times stronger than that for the undoped beam. This suggests that doping of the mesoscopic beams was accompanied by structural disorder. The peak at around 10 K in the conductivity-temperature curve for the bulk sample has shifted to a much higher value of around 60 K for the nanobeams. The conductivity of the undoped nanobeam merges with the conductivity of bulk above the Debye temperature (345 K) of GaAs. However, the conductivity of the doped nanobeams continues to remain lower than that of the undoped nanobeam for all temperatures up to at least 1,000 K.

3.4.3 Si Nanowires

In the previous subsection we showed that the Debye–Callaway model of lattice thermal conductivity, developed for bulk solids, can be successfully applied to explain the conductivity results for GaAs beams of cross-sectional dimensions in the range of 100–250 nm. Phonon transport in thin quasi-one-dimensional structures, such as thin nanowires with cross-sectional dimensions smaller than 50 nm, is likely to be sensitive to both surface roughness and quantum confinement effects. There have been several theoretical attempts for explaining experimentally measured thermal conductivity results of Si nanowires, including the semi-classical Boltzmann-type approach [41], a semi-empirical molecular dynamics approach [42], and the quantum Landauer formalism [43]. All these models are capable of explaining the measured thermal conductivity [44] of Si nanowires of thicknesses (diameters) 115, 56, and 37 nm. However, it has been argued [43] that in order to explain the conductivity of the nanowire of diameter 22 nm it is important to employ a theoretical model that combines incoherent surface scattering for short-wavelength phonons with nearly ballistic long-wavelength phonons. However, in a recent work [45] we have argued that Callaway's relaxation-time model for thermal transport in bulk materials, described at the start of this section, can be successfully applied to explain the measurements for Si nanowires with cross-sectional dimensions down to 22 nm.

Calculations were made with the following parameters for Si nanowires of diameters 115, 56, 37, and 22 nm, respectively: effective boundary length values of 0.115, 0.056, 0.037, 0.010 μm; effective mass-defect scattering parameter A_{md} (see Eq. (3.27)) values of 45.0×10^{-46} s^3, 45.0×10^{-46} s^3, 250.0×10^{-46} s^3, 500.0×10^{-46} s^3; Grüneisen's constant values of 1.4, 1.7, 1.7, 1.7. Figure 3.8 clearly shows that there is reasonably good agreement between the presently calculated results and the experimental measurements for Si nanowires of all the four thicknesses studied by Li et al. [44]. For reproducing the experimental results for the nanowires of diameters 115 nm and 56 nm we had to use several times stronger mass-defect scattering parameter than what is needed for bulk Si. For the thinner nanowire of diameter 37 nm, the mass-defect parameter had to be increased five-fold compared to that for the thicker nanowires. For the thinnest nanowire (diameter 22 nm) we had to consider a very strong diffused surface (boundary) scattering, and a mass defect scattering parameter twice that for the 37 nm wire. The choice of significantly smaller effective boundary length for the 22 nm wire clearly indicates that surface of this wire is quite rough. We also note that for nanowires of all thickness, we had to use a stronger anharmonicity factor (Grünisen's constant γ) than is needed for bulk Si (usually $\gamma = 0.8$ is adequate). Following the discussion in the theory section, we re-iterate that the level of successful agreement between theory and experiment for the conductivity achieved for the 22 nm nanowire is not expected to continue to much thinner nanowires.

Three clear trends can be noticed. Firstly, the maximum of the conductivity generally shifts to higher temperatures with decrease in the nanowire thickness. This is due to the joint effect of strong boundary and strong mass defect scatterings

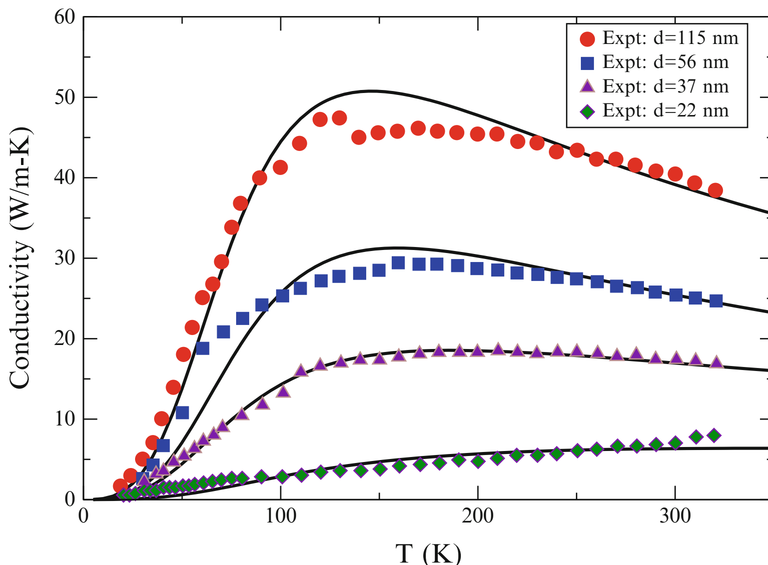

Fig. 3.8 Thermal conductivity of (**a**) Si bulk and (**b**) Si nanowires: theory (*lines*); experiment [44] (*symbols*). Taken from [45] (NWs)

of phonons. Secondly, for temperatures up to well over the room temperature the conductivity of nanowires has been reduced by 2–3 orders of magnitude with respect to the bulk values. A similar conclusion has been reached from another theoretical investigation [42]. Thirdly, at a given (low) temperature, the conductivity decreases with the decrease in nanowire thickness. A definite relationship for the decrease in the conductivity with nanowire thickness is difficult to establish, as the surface and interior qualities are not guaranteed to be maintained during nanowire fabrication.

3.4.4 Si/Ge Superlattices

The lattice thermal conductivity of superlattices has been reported to be at least two orders of magnitude lower than that of constituent bulk materials [46, 47]. What mechanisms govern the low thermal conductivity of superlattices is not generally well understood. Let us consider a superlattice of repeat period thickness $d = d_1 + d_2$, containing two components of thicknesses d_1 and d_2. Let us further consider that the Landau–Peirls–Ziman condition in Eq. (3.18) is satisfied. This can be interpreted as the superlattice sample size L being larger than the phonon mean free path Λ. We note that the sample size L contains several multiples of the superlattice unit cell size d, so that $L = Nd$ with N ranging from about 10–1,000

for typically grown samples. With this understanding, one can distinguish three regimes of phonon transport along the superlattice growth direction [48]:

(i) For superlattices with $d \gg \Lambda$, the thermal conductivity κ can be fairly well expressed as

$$1/\kappa = (d_1/\kappa_1 + d_2/\kappa_2)/(d_1 + d_2), \tag{3.54}$$

where κ_i is the conductivity of the ith bulk material;

(ii) For superlattices with $d \sim \Lambda$,

$$1/\kappa = (d_1/\kappa_1 + d_2/\kappa_2 + 2W_K)/(d_1 + d_2), \tag{3.55}$$

where W_K is the Kapitza resistance of the superlattice interface;

(iii) For $d \ll \Lambda$, it will be important to consider the superlattice as a single new material and a detailed consideration of phonon group velocities, phonon density of states, and phonon lifetime will be required for thermal conductivity calculations.

Here we will discuss the phonon conductivity of thin Si/Ge superlattices (i.e. for case (iii): $d \ll \Lambda$). As discussed in Sect. 3.3.1.2, the phonon dispersion relations in thin Si/Ge superlattices are significantly different from those in bulk Si or Ge. These changes lead to reduction in the speeds of acoustic phonons and changes in the density of states. Although such changes can be manipulated to some extent by altering the superlattice period and layer thicknesses, the resulting changes would not be enough to explain the reduced thermal conductivity of the superlattices. With the help of the numerically obtained results for phonon group velocities, density of states and phonon relaxation times, we provide a plausible explanation for this by considering numerical results for two specific choices of Si/Ge superlattices, Si(19)/Ge(5)[001] and Si(72)/Ge(30)[001], as fabricated and studied by Lee et al. [46].

Equation (3.19) was used to express the components of the conductivity tensor, with axes along [$\bar{1}$10], [110], and [001]. Numerical results for phonon dispersion curves and density of states were obtained by employing an enhanced adiabatic bond charge model [18]. Phonon scattering rates due to point mass defects, interface mass-mixing (IMS), interface dislocations (IDS), and anharmonic interactions were calculated using Eqs. (3.26), (3.33), (3.35), and (3.45), respectively. The amplitude ratio e_B/e_A was calculated using Eq. (3.36). The required BZ summations were carried out using the special $\boldsymbol{q}$-points scheme as described in Sect. 3.3.2. However, the IMS and IDS parameters α and α' had to be treated as adjustable parameters. This became necessary due to the fact that no information is available for the amount of mass mixing and the nature and concentration of interface dislocations, except that these features are always present during the growth of Si/Ge systems [49].

The numerically calculated results for the lattice thermal conductivity of the two superlattices, along the growth direction, are presented in Fig. 3.9. Also presented are the experimentally measured results, obtained by Lee et al. [46]. In order to fit

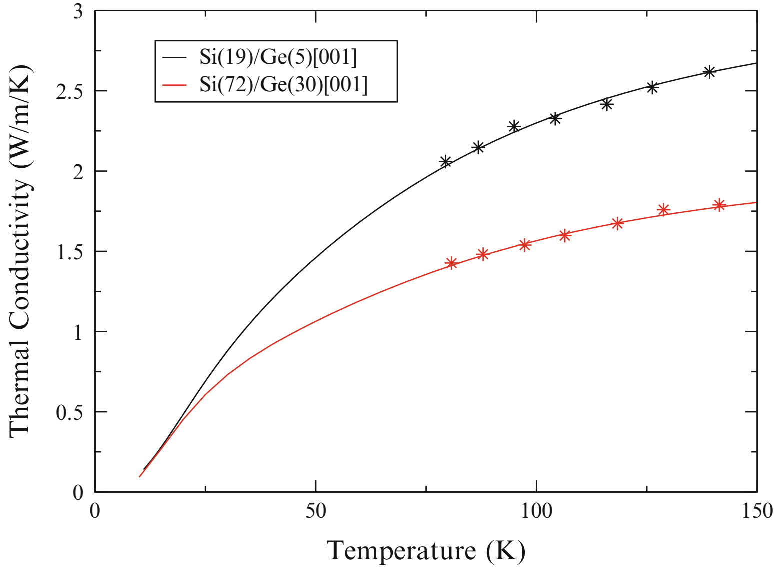

Fig. 3.9 Thermal conductivity of Si/Ge superlattices along [001], the growth direction: theory [29] (*lines*), experiment [46] (*symbols*). Reproduced from [29]

the experimentally measured numerical results and the temperature variation of the conductivity up to 150 K, the role of phonon anharmonic interactions was found to be unimportant. While in the boundary scattering region there is essentially no difference in the conductivity of the two samples, at higher temperatures the lower conductivity in the (72,30) superlattice is due to the dominant IDS mechanism. Indeed, it was found that for the thinner superlattice IMS is the dominant scattering mechanism (with $\alpha = 550$) and the contribution from IDS is negligible ($\alpha' = 0$). For the thicker superlattice both IMS and IDS mechanisms are significant, but IDS dominates ($\alpha \simeq 10^7$ and $\alpha' \simeq 10^{-4}$).

The thermal conductivity of both the Si/Ge superlattices studied here is much lower compared to the conductivities of bulk Si or Ge. This is generally true of both the peak value of the conductivity and of the value at any temperature. This can be ascertained from an examination of the bulk results presented in Fig. 3.6 and the superlattice results presented in Fig. 3.9. At 100 K, the conductivity of the superlattices is three orders of magnitude smaller than the average of the conductivities of the bulk materials. It is interesting to note that at 100 K, the conductivity of the Si nanowires (cf. Fig. 3.8) is also three orders of magnitude smaller than the bulk conductivity in Si. However, the physical reasons for the reduction in the conductivity values in the superlattice and nanowire structures are different. The reduction in the conductivity of the Si nanowires is due to the phonon boundary scattering mechanism. In contrast, the reduction in the conductivity of the Si/Ge superlattices is due to a combined effects of reduced phonon velocity, stronger anharmonic interactions (consistent with larger periodicity), and phonon interface scattering mechanisms.

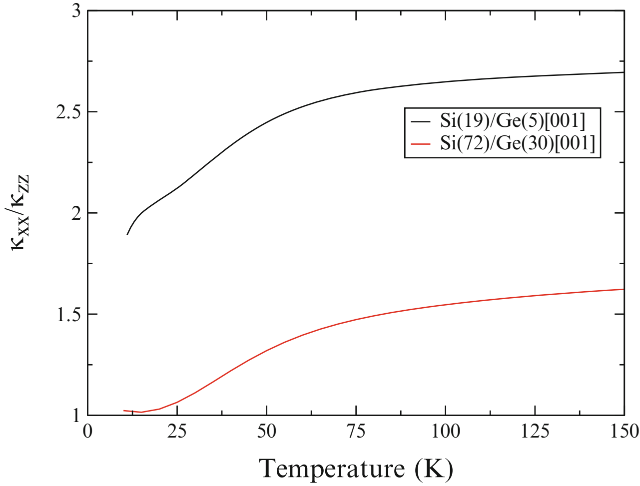

Fig. 3.10 The thermal conductivity ratio κ_{xx}/κ_{zz} for two Si/Ge superlattices as a function of temperature

While the conductivity in the bulk materials is essentially isotropic, it shows a clear anisotropic behaviour in the superlattice structure. Figure 3.10 shows the numerically obtained values of the conductivity in the superlattice plane (κ_{xx}) and along the superlattice growth direction (κ_{zz}). At low temperatures, the ratio κ_{xx}/κ_{zz} tends to unity for the thicker superlattice, but remains larger than unity for the thinner superlattice. This difference in the low-temperature ratio κ_{xx}/κ_{zz} arises due to different behaviours of the IMS and IDS mechanisms in thinner and thicker superlattices. Only low-lying phonon modes are appreciably populated at low temperatures. Also, as discussed earlier, zone-edge modes are more strongly scattered than zone-centre modes. For the thinner superlattice, with less zone-folding, the zone edge modes are not populated until higher temperatures. In contrast, in the thicker superlattice, there is a larger amount of zone folding, lending to population of a larger number of phonon modes both at the zone centre and at the zone edge. Thus, both the IMS and IDS mechanisms become more anisotropic for the thinner superlattice than for the thicker superlattice.

3.5 Concept of Phonon Engineering of Thermoelectric Materials

Thermoelectricity (TE) is the process of generating either electricity from heat engines or heating devices from electricity. Examples of modern TE applications include portable refrigerators, beverage coolers, electronic component coolers, infrared sensing, etc. Possible future applications of TE devices include efficient

conversion of waste heat (e.g. from waste and during powering of vehicles) into usable energy, improving efficiency of photovoltaic cells, etc. Thermoelectric materials have been investigated for several decades due to their energy efficiency. The efficiency of thermoelectric materials is defined by the figure of merit quantity ZT given by $ZT = S^2\sigma T/\kappa$, where S is the Seebeck coefficient (a measure of conversion of temperature difference into electricity), σ is the electrical conductivity, and κ is the thermal conductivity. Larger values of ZT require high S, high σ, and low κ. After decades of research it has been established that alloyed semiconductors with high carrier concentration are the most efficient TE bulk materials.

The thermal conductivity κ of semiconducting materials can be contributed by carriers (donor electrons or acceptor holes in doped samples), lattice (or phonons), and electron–hole pairs (bipolar contribution in intrinsic semiconductors): $\kappa = \kappa_{\mathrm{el}} + \kappa_{\mathrm{ph}} + \kappa_{\mathrm{bp}}$. An increase in S normally implies a decrease in σ because of carrier density considerations, and an increase in σ normally implies an increase in κ_{el} (as given by the Wiedemann–Franz law). The bipolar contribution κ_{bp} increases rapidly above temperatures corresponding to thermal energy larger than the semiconductor band gap. Thus, it is very difficult to increase ZT in typical bulk semiconductor TE materials. Clearly, for high values of ZT, we require materials which are characterised by less efficient scattering of carriers (to increase σ) and efficient scattering of phonons (to reduce κ). From research over the past several decades it has been found that semiconductor bulk alloys such as SiGe and BeTeSe, and PbTeS are amongst the most promising TE materials. In fact, SiGe are good high-temperature TE materials [50] and bismuth chalcogenides (e.g. BiTeSe) are good low-temperature TE materials [51]. Good reviews of the current status can be found in [52–54]. For most bulk materials the room-temperature ZT has been found to be less than 1. However, there is a report of $ZT = 2$ at $T = 800$ K for $\mathrm{AgPb}_m\mathrm{SbTe}_{2+m}$ [55].

Several theoretical and computational attempts have been made to obtain numerically accurate estimates of the TE coefficients σ, S, κ_{el}, κ_{bp}, and κ_{ph}. In order to compute σ, S, and κ_{el} at different temperatures it is important first to compute Fermi level both in extrinsic (carrier controlled) and intrinsic (host controlled) temperature ranges [56]. With that information being available, the nearly free electron theory can reasonably well be applied to compute σ, S, and κ_{el}. Useful expressions can be found in [57, 58]. The coefficient κ_{bp} is usually computed using the Price theory [59]. The theory discussed in this chapter can be used to compute κ_{ph}. Interested readers are referred to [30, 60–62] for details.

In recent years efforts have started to overcome the challenge of developing materials with $ZT > 3$. Such efforts have concentrated on creating new semiconducting materials. Two primary approaches are being considered: formation of complex crystal structures or fabrication of reduced-dimensional (especially nanostructured) materials. Reduced-dimensional systems can be categorised as 2D structures (i.e. thin films), 1D structures (i.e. nanowires), or 0D structures (i.e. quantum dots). Nanostructures can also be fabricated using two or more materials (known generally as nanocomposites), such as superlattices of alternating layers of two materials, an array of nanowires of one material embedded in another host, and an array of

nanodots of one material embedded in the host of another material. Theoretical modelling suggests [58] that a Bi_2Te_3 quantum-well structure has the potential to increase ZT by an order of magnitude over the bulk value. Although Si is a poor thermoelectric material, arrays of rough Si nanowires of diameter in the range 20–300 nm are found to exhibit $ZT = 0.6$ at room temperature [63]. Recently, it has been found that stacks of thin films of Bi_2Te_3 exhibit enhanced ZT [64]. In particular, it has been theoretically suggested that quintuple atomic layers of Bi_2Te_3 can exhibit $ZT = 7.15$ [65].

It is exciting to think that in general fabrication of reduced-dimensional structures, in particular nanocomposite structures, can be tailored to exhibit much reduced lattice (phonon) conductivity, thus leading to an enhancement in ZT. However, a detailed and accurate investigation of an enhancement in ZT of nanocomposites will require knowledge of phonon dispersion relations and phonon scattering processes and their relative strengths. In particular, for nanowires and nanodots phonon scattering at rough boundaries is likely to play a dominant role. For superlattices, as discussed earlier in this chapter, interface scattering and enhanced anharmonic interaction due to the onset of mini-Umklapp processes and the dual mass term will play a dominant role in reducing the phonon lifetime and thus the thermal conductivity. The theoretical developments in Sect. 3.3.3.3 have indicated how to deal with phonon interface scatterings. Due to our poor understanding of temperature-dependent crystal anharmonic forces and the resultant phonon–phonon scattering strength, accurate calculations of phonon conductivity is, at least at present, essentially a very difficult problem even for single crystal semiconductors. In Sect. 3.3.3.4 in this chapter we have indicated how the concept of phonon anharmonic interactions in bulk can be extended to the case of a superlattice. These ideas can be modified and extended to deal with phonon scattering rates in nanocomposites in general. With the help of accurate determination of phonon lifetimes and phonon conductivity κ_{ph} for various types and sizes of nanocomposites it would be possible to develop the concept of phonon engineering for efficient TE materials.

3.6 Summary

In this chapter we have reviewed some of the existing theories of phonon transport in bulk and nanostructured solids. Particular attention has been paid to a detailed description of the essential steps required in the derivation and numerical evaluation of the thermal conductivity within the single-mode and an effective-mode phonon relaxation time approximations. Lattice thermal conductivity results have been presented for bulk Si, Ge, and GaAs, for suspended nanobeams of GaAs, for Si nanowires, and for Si/Ge superlattices.

It has been shown that the effect of reduction in dimensionality of a material results in significant reduction in its lattice thermal conductivity. Reduction of up to three orders of magnitude has been noted for thin Si nanowires (quasi

one-dimensional structures) and thin Si/Ge superlattices (quasi two-dimensional structures). It has been explained that the physical reasons behind the same amount of reduction in the conductivity due to the Si/Ge superlattice and Si nanowire formations are different. Another significant effect of reduction in dimensionality is to change the isotropic nature of the conductivity into a tensor quantity. This has been illustrated from numerical calculations for Si/Ge superlattices. It has been explained that the anisotropic nature of the conductivity is more pronounced in thinner superlattices.

Finally, it has been pointed out that a huge reduction in the lattice thermal conductivity can be achieved by the formation of nanostructured semiconductors, resulting into the possibility of significant enhancement in thermoelectric figure of merit. Such an enhancement can be achieved, within reasons, by employing the concept of phonon engineering of nanocomposite semiconductors: i.e. by reducing the velocities and lifetimes of thermally active phonon modes by fabricating nanostructures of different shapes and sizes.

Acknowledgements I wish to thank my past and present Ph. D. students and postdoctoral fellows for their contribution towards the development of the subject matter presented here. Special thanks to Ceyda Yelgel for careful reading of the manuscript. This work has been supported by EPSRC (UK) through the grant number EP/H046690.

References

1. Kubo R (1957) J Phys Soc Jpn 12:570
2. Ziman JM (1960) Electrons and phonons. Clarendon, Oxford
3. Srivastava GP (1990) The physics of phonons. Adam Hilger, Bristol (now Taylor and Francis Group)
4. McGaughey AJH, Kaviany M (2004) Phys Rev B 69:094303
5. Kaburaki H, Yip S, Kimizuka H (2007) J Appl Phys 102:043514
6. Huang B-L, Kaviany M (2008) Phys Rev B 77:125209
7. Ziman JM (1969) Elements of advanced quantum thoery. Cambridge University Press, Cambridge
8. Guyer RA, Krumhansl JA (1966) Phys Rev 148:766
9. Benin D (1970) Phys Rev B 1:2777
10. Srivastava GP (1976) J Phys C Solid State Phys 9:3037
11. Srivastava GP (1976) J Phys C Solid State Phys 10:1843
12. Arthurs AM (1970) Complementary variational principles. Clarendon, Oxford
13. Carruthers P (1961) Rev Mod Phys 33:92
14. Callaway J (1959) Phys Rev 113:1046
15. Srivastava GP (1976) Phil Mag 34:795
16. Weber W (1977) Phys Rev B 15:4789
17. Tütüncü HM, Srivastava GP (1996) Phys Rev B 53:15675
18. Hepplestone SP, Srivastava GP (2008) Phys Rev Lett 101:105502
19. Baroni S, de Gironcoli S, Dal Corso A, Giannozzi P (2001) Rev Mod Phys 73:515
20. Dolling G (1963) Inelastic scattering of neutrons in solids and liquids, vol I. IAEA, Vienna, p 37
21. Nilsson G, Nelin G (1972) Phys Rev B 6:3777

22. Ezzahri Y, Grauby S, Rampnoux JM, Michel H, Pernot G, Claeys W, Dilhaire S, Rossignol C, Zeng G, Shakouri A (2007) Phys Rev B 75:195309
23. Hepplestone SP, Srivastava GP (2006) Nanotechnology 17:3288
24. Chadi DJ, Cohen ML (1973) Phys Rev B 8:5747
25. Monkhorst HJ, Pack JD (1976) Phys Rev B 13:5189
26. Holland MG (1964) Phys Rev 134:A471
27. Kim W, Majumdar A (2006) J Appl Phys 99:084306
28. Gillet J-N, Chalopin Y, Volz S (2009) J Heat Transfer 131:043206
29. Hepplestone SP, Srivastava GP (2010) Phys Rev B 82:144303
30. Thomas IO, Srivastava GP (2012) Phys Rev B 86:045205
31. Parrott JE (1971) Phys Status Solid B 48:K159
32. Ren SY, Dow JD (1982) Phys Rev B 25:3750
33. Ziman JM (1956) Phil Mag 1:191
34. Ziman JM (1957) Phil Mag 2:292
35. Parrott JE (1979) Rev Int Hautes Tem Refract 16:393
36. Holland MG, Neuringer LJ (1962) In: Proc. Int. congr. on the physics of semiconductors, exeter, Institute of Physics, London, p 475
37. Geballle TH, Hull GW (1958) Phys Rev 110:773
38. Srivastava GP (1980) J Phys Chem Solid 41:357
39. Fon W, Schwab KC, Worlock JM, Roukes ML (2002) Phys Rev B 66:045302
40. Barman S, Srivastava GP (2006) Phys Rev B 73:205308
41. Walkauskas SG, Broido DA, Kempa K, Reinecke TL (1999) J Appl Phys 85:2579
42. Volz SG, Chen G (1999) Appl Phys Lett 75:2056
43. Murphy PG, Moore JE (2007) Phys Rev B 76:155313
44. Li D, Wu Y, Kim P, Shi L, Yang P, Majumdar A (2003) Appl Phys Lett 83:2934
45. Srivastava GP (2009) Mat Res Soc Symp Proc 1172:T08-07
46. Lee SM, Cahill DG, Vekatasubramanian R (1997) Appl Phys Lett 70:2957
47. Cahill DG, Ford WK, Goodson KE, Mahan GD, Majumdar A, Maris HJ, Merlin R, Phillpot SR (2003) J Appl Phys 93:793
48. Capinski WS, Maris HJ, Ruf T, Cardona M, Ploog K, Katzer DS (1999) Phys Rev B 59:8105
49. Mo Y-W, Savage DE, Swartzentruber BS, Lagally MG (1990) Phys Rev Lett. 65:1020; Ma T, Tu H, Shao B, Liu A, Hu G (2006) Mater Sci Semicond Process 9:49
50. Dismukes JP, et al (1964) J Appl Phys 35:2899; Heddins HR, Parrott JE (1976) J Phys C Solid State Phys 9:1263
51. Goldsmid HJ (1964) Thermoelectric refrigeration. Plenum, New York; Goldsmid HJ (1986) Electronic refrigeration. Pion, London
52. Venkatasubramanium R, Siivola E, Colpitts T, O'Quinn B (2001) Nature 413:697
53. Majumdar A (2004) Science 303:777
54. Minnich AJ, Dresselhaus MS, Ren ZF, Chen G (2009) Energy Environ Sci 2:466
55. Hsu KF, Loo S, Guo F, Chen W, Dyck JS, Uher C, Hogan T, Polychroniadis EK, Kanatzidis MG (2004) Science 303:818
56. McKilvey JP (1966) Solid state and semiconductor physics (International edition). Harper & Row, New York-Evanston-London, and John Weatherhill, Tokyo
57. Drabble JR, Goldsmit HJ (1961) Thermal conduction in semiconductors. Pergamon Press, Oxford, pp 115–117
58. Hicks LD, Dresselhaus MS (1993) Phys Rev B 47:12727
59. Price PJ (1955) Phil Mag 46:1252
60. Vining CB (1991) J Appl Phys 69:331
61. Minnich AJ, Lee H, Wang XW, Joshi G, Dresselhaus MS, Ren ZF, Chen G, Vashaee D (2009) Phys Rev B 80:155327
62. Yelgel ŎC, Srivastava GP (2012) Phys Rev B 85:125207
63. Hochbaum A, Chen R, Deigado RD, Liang W, Garnett EC, Najarian M, Majumdar A, Yang P (2008) Nature 451:163
64. Goyal V, Teweldebrhan D, Balandin AA (2010) Appl Phys Lett 97:133117
65. Zahid F, Lake R (2010) Appl Phys Lett 97:212102